JOURNAL OF GEOPHYSICAL RESEARCH, VOL. 115, A08226, doi:10.1029/2009JA014389, 2010

Saturation of polar cap potential: Nonlinearity in quasi-steady solar wind-magnetosphere-ionosphere coupling

J. R. Kan,[1,2] H. Li,[1] C. Wang,[1] B. B. Tang,[1] and Y. Q. Hu[3]

Received 24 April 2009; revised 15 November 2009; accepted 4 March 2010; published 27 August 2010.

[1] We propose a quasi-steady nonlinear circuit model for the solar wind-magnetosphere-ionosphere (SW-M-I) coupling to study the observed saturation of polar cap potential. The oval conductance is shown to be a nonlinear circuit element since it increases with increasing dayside reconnection *E* field driving the proposed circuit. Oval conductance is produced by precipitating particles energized by enhanced sunward convection in the plasma sheet driven by reconnection at the dayside magnetopause and in the plasma sheet. The asymptotic saturation potential is shown to increase with (1) decreasing internal resistance of the dynamo region, (2) increasing length of dayside reconnection line, (3) increasing ratio of nightside to dayside reconnection potentials, and (4) increasing ratio of nightside to dayside internal resistances.

Citation: Kan, J. R., H. Li, C. Wang, B. B. Tang, and Y. Q. Hu (2010), Saturation of polar cap potential: Nonlinearity in quasi-steady solar wind-magnetosphere-ionosphere coupling, *J. Geophys. Res.*, *115*, A08226, doi:10.1029/2009JA014389.

1. Introduction

[2] The solar wind-magnetosphere-ionosphere (SW-M-I) coupling is fundamental to understanding substorms and storms. A characteristic difference between substorms and storms is the distinct difference of their time scales. Substorm time scale is less than a few hours, while storm time scale is greater than several tens of hours.

[3] The cause of polar cap potential saturation is not well understood despite extensive observations, theoretical modeling, and simulation studies. To gain an insight into the polar cap potential saturation problem, we refer the reader to a comprehensive review by *Shepherd* [2007].

[4] Observations show that the value at which the polar cap potential saturates appears to depend on the conductance in the ionosphere. The polar cap saturation potential is around ~100 to ~200 kV when the reconnection *E* field imposed by the solar wind exceeds ~10 mV/m [*Reiff et al.*, 1981; *Doyle and Burke*, 1983; *Reiff and Luhmann*, 1986; *Boyle et al.*, 1997; *Russell et al.*, 2001; *Shepherd et al.*, 2003; *Hairston et al.*, 2005; *MacDougall and Jayachandran*, 2006; *Lockwood et al.*, 2009]. *Russell et al.* [2001] use the AMIE model to infer polar cap potential of five storms to demonstrate the polar cap potential saturation for solar wind *E* field up to ~10 mV/m. *Shepherd et al.* [2003] analyzed Super Dual Auroral Radar Network (SuperDARN) data to determine the statistical characteristics of polar cap potential saturation for the solar wind *E* field up to ~17 mV/m and showed evidence for saturation starting at ~3 mV/m. *Hairston et al.* [2003, 2005] used data from the DMSP-F13 spacecraft during three superstorms to show that the polar cap potential saturation reaches the asymptotic saturation potential of ~150 kV when the solar wind *E* field increases from ~10 to ~40 mV/m.

[5] Theoretical and simulation studies of polar cap potential saturation have been conducted extensively [*Hill*, 1984; *Fedder and Lyon*, 1987; *Siscoe et al.*, 2002, 2004; *Ridley*, 2005; *Merkin et al.*, 2005; *Kivelson and Ridley*, 2008]. Despite these efforts, the cause of polar cap potential saturation is still not well understood. Most popular among the various proposed models is the Hill-Siscoe model [*Hill*, 1984; *Siscoe et al.*, 2002, 2004]. They proposed an intriguing interpretation that polar cap potential saturation is caused by the transition from the Chapman-Ferraro closed magnetosphere to the Dungey-Alfvén open magnetosphere. The CF current system dominates the CF mode of interaction with the solar wind, while the region 1 current system dominates the DA mode of interaction. In other words, the observed PC potential saturation in the Hill-Siscoe model is caused by transition from CF dominance to DA dominance. Simulation models of *Fedder and Lyon* [1987], *Merkin et al.* [2005], and *Ridley* [2005] show that the polar cap potential saturates at a lower level with a higher ionospheric conductivity. In short, observations, simulations, and theories all indicate that the saturation of polar cap potential is invariably related to the conductance in the ionosphere.

[6] Circuit models have been proposed by many to study substorm problems where electric currents play a vital role. *Sato and Holzer* [1973] proposed a circuit model to study the quiet auroral arcs in the M-I coupling. *Siscoe* [1982] proposed a circuit model to study the energy coupling between

[1]State Key Laboratory of Space Weather, Center for Space Science and Applied Research, Chinese Academy of Sciences, Beijing, China.
[2]Geophysical Institute, University of Alaska Fairbanks, Fairbanks, Alaska, USA.
[3]CAS Key Laboratory of Basic Plasma Physics, School of Earth and Space Sciences, University of Science and Technology of China, Hefei, Anhui, China.

0148-0227/10/2009JA014389

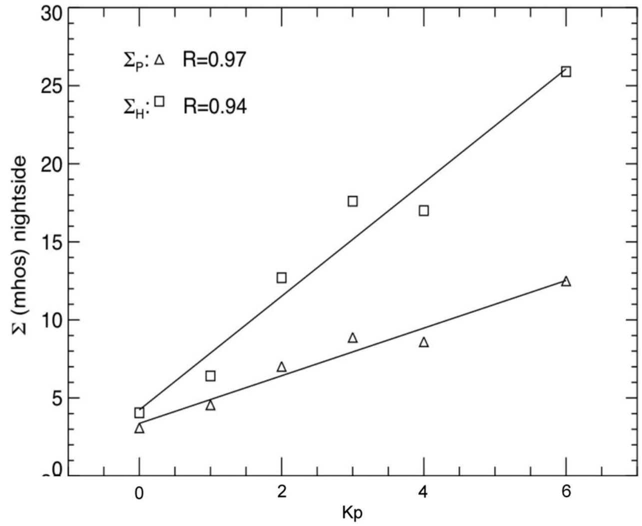

Figure 1. The Hall and Pedersen conductance Σ_H and Σ_P in the ionosphere deduced from DMSP data by *Hardy et al.* [1987] are plotted against K_P.

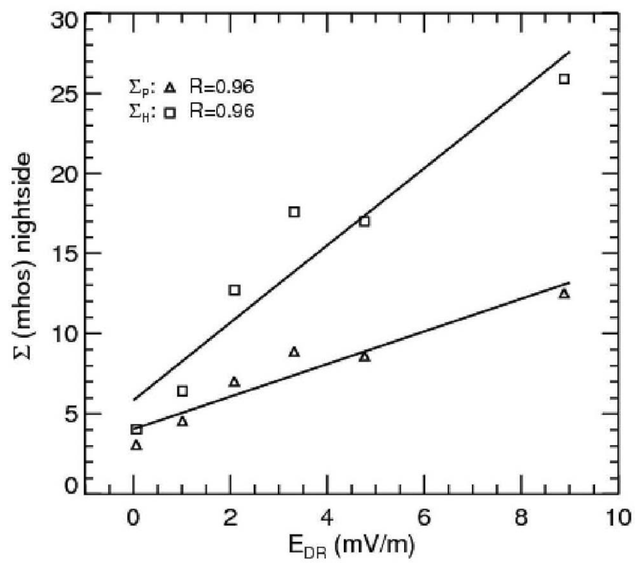

Figure 3. Combining Figures 1 and 2, the observed conductance Σ_H and Σ_P versus E_{DR} up to E_{DR} ~ 9 mV/m.

regions 1 and 2 of Birkeland current systems. *Liu et al.* [1988] proposed a time-dependent circuit model with resistance, inductance, and capacitance to describe substorms. *Block et al.* [1998] considered a time-dependent circuit model consists of inductance and capacitance for treating the substorm breakup problem.

[7] In the present paper, we propose a quasi-steady nonlinear circuit model of SW-M-I coupling to study the observed PCP saturation on the storm time scale of few tens of hours or more. Inductance and capacitance can be omitted in a quasi-steady circuit model. We emphasize in the proposed model that the observed polar cap potential saturation originates from the oval conductance as a nonlinear circuit element, which is shown to increase with increasing dayside reconnection electric field driven by the solar wind. The asymptotic saturation potential is predicted to depend on the internal resistance in the dynamo region, the length of dayside reconnection line, the ratio of dayside/nightside reconnection potentials, and the ratio of dayside/nightside internal resistances of the reconnection region.

2. Observations of Oval Conductance and Polar Cap Potential

[8] *Hardy et al.* [1987] obtained Pedersen and Hall conductance in the ionosphere from the precipitating electron and ion fluxes measured by the DMSP spacecraft. Figure 1 plots the conductance thus obtained for $K_P \leq 6$.

[9] Figure 2a shows the scatterplot of max K_P versus max E_{DR}, during a magnetic storm for 227 storms from 1998 to 2005, derived in the present paper. The K_P index is obtained from http://swdcwww.kugi.kyoto-u.ac.jp. The dayside reconnection E field E_{DR} is calculated from the observations of ACE by using the formula in *Kan and Lee* [1979],

$$E_{DR} = V_X B_{YZ} \sin^2(\theta/2), \tag{1}$$

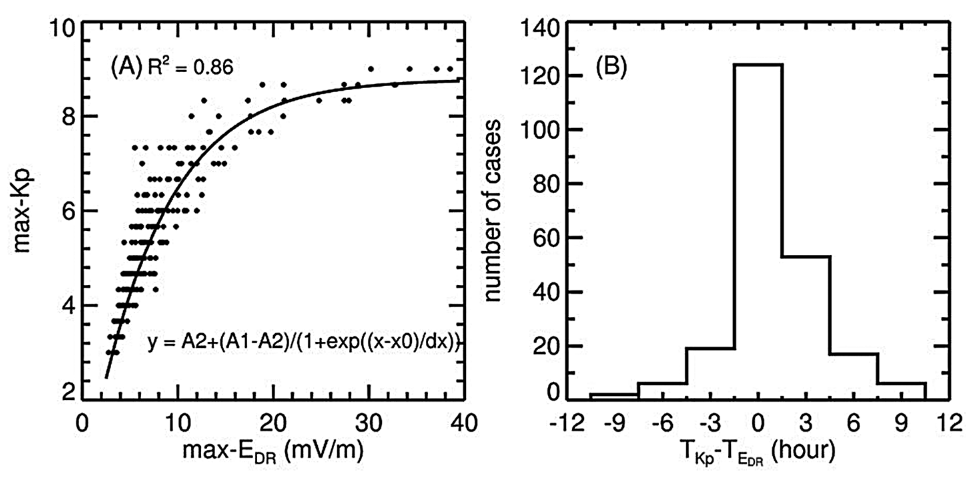

Figure 2. The observed scatterplot K_P versus E_{DR} is the key to transforming the observed conductance versus K_P [*Hardy et al.*, 1987] to conductance versus E_{DR}.

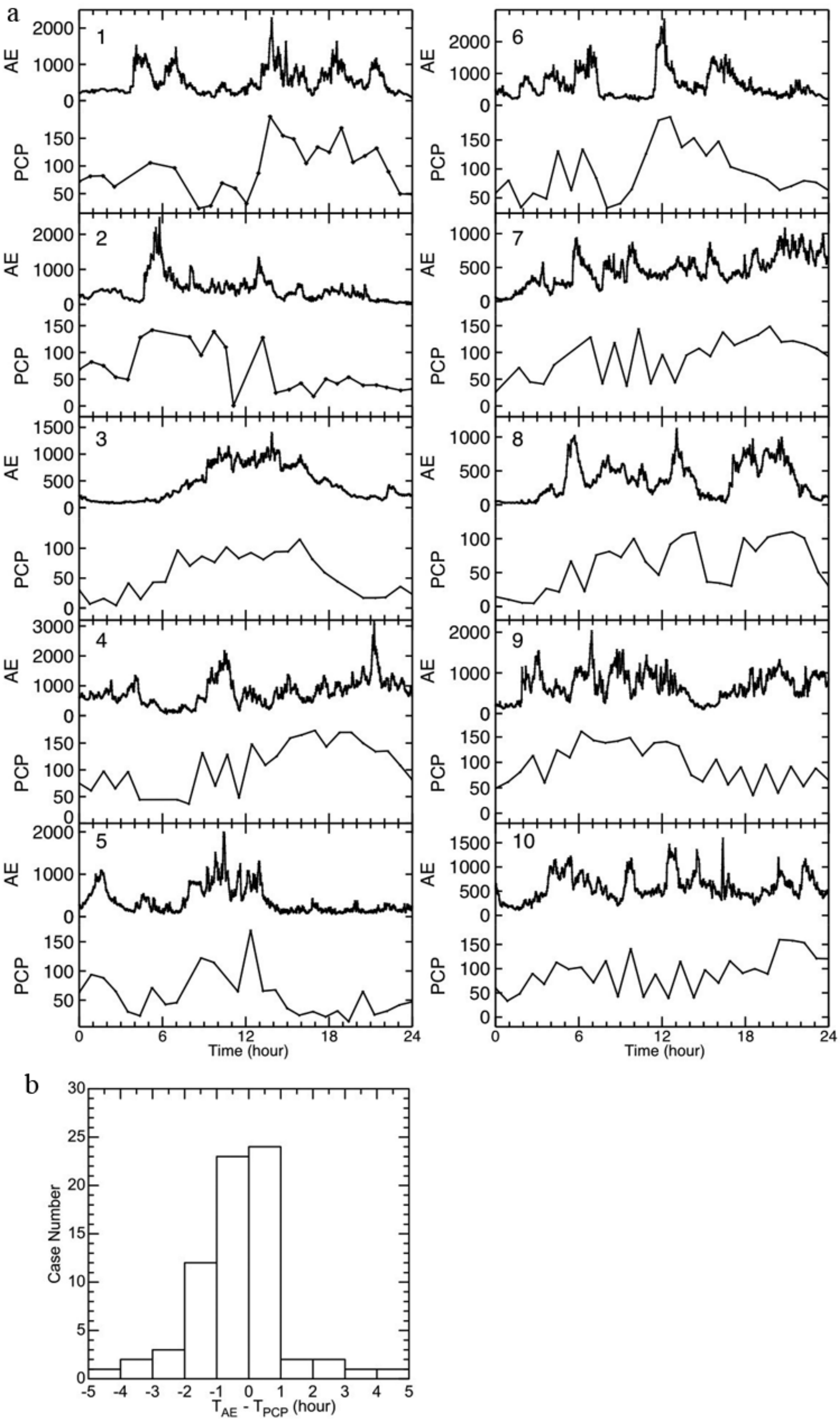

Figure 4. (a) Comparison of the time series of AE and PCP during each of the 10 examples of storms. (b) The occurrence time difference between max AE and max PCP for the 71 storms chosen for this study.

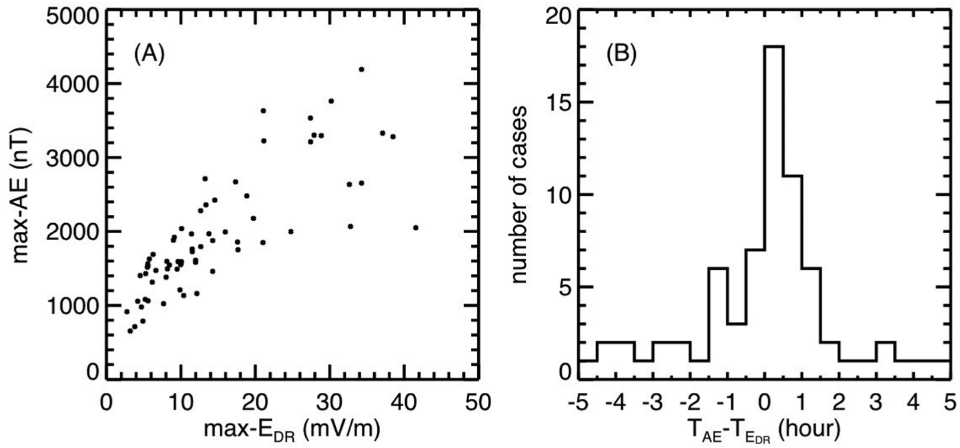

Figure 5. (a) Scatterplot of max AE versus max E_{DR} for the 71 storm events. The dashed line is a linear fitting of the scatterplot with correlation coefficient $R = 0.8$. (b) The distribution of occurrence time difference between max AE and max E_{DR} for the 71 storm events.

where V_X is the solar wind speed, B_{YZ} is the IMF Y-Z component, and θ is the IMF clock angle in the Y-Z plane. In calculating E_{DR}, we have already included the propagating time from ACE to the magnetopause, using the observed solar wind velocity. The temporal resolution of K_P index is 3 h and that of E_{DR} is 64 s. The procedure of derivation is discussed as follows. During each storm, K_P increases towards the maximum value max K_P at T_{KP}, as E_{DR} increases towards the maximum value max E_{DR} at T_{EDR}. Figure 2b shows the distribution of occurrence time difference $T_{KP} - T_{EDR}$. Distribution of the occurrence time difference is shown to fall within ~±3 h.

[10] Combining results in Figures 1 and 2, we obtain Pedersen and Hall conductance versus E_{DR} as shown in Figure 3. The range for Σ_P versus E_{DR} in Figure 3 is limited to $E_{DR} \leq$ ~9 mV/m.

[11] Extension of E_{DR} in Figure 3 from ~9 to ~40 mV/m is discussed later in connection with Figures 4, 5, 6, and 7.

[12] The AE index is a measure of auroral electrojet I_O flowing in the oval as given by

$$I_O = \alpha \mathrm{AE}. \quad (2)$$

The parameter α is a scaling constant to be determined later in Figure 7. The electrojet current can be written as

$$I_O = \Sigma_O \Phi_{PC}. \quad (3)$$

The oval conductance Σ_O is Pedersen conductance under quiet conditions; it is enhanced to Cowling conductance under disturbed conditions during substorms and storms [*Kan*, 2007]. Substituting (3) into (2), the oval conductance can be written as

$$\Sigma_O = \alpha \mathrm{AE}/\Phi_{PC}. \quad (4)$$

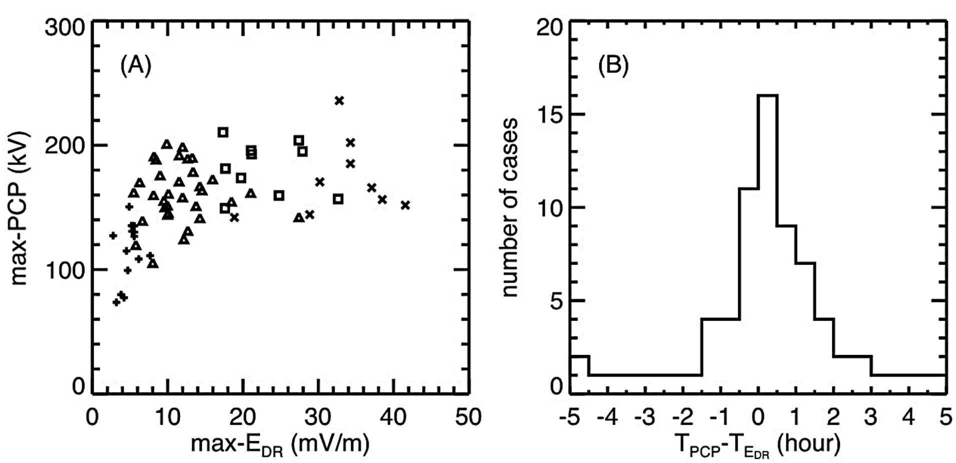

Figure 6. (a) Scatterplot of max Φ_{PC} versus max E_{DR} of the same 71 magnetic storms. The reconnection E field data are based on data obtained from ACE spacecraft. Small to moderate storms with SYMH between −50 and −100 nT are denoted by the black plus signs; moderate to big storms with SYMH between −100 and −200 nT are denoted by triangles; big to intense storms with SYMH between −200 and −300 nT are denoted by squares; intense to super storms with SYMH between −300 and −500 nT are denoted by crosses. (b) The time difference between max PCP and max E_{DR} for the 71 storms.

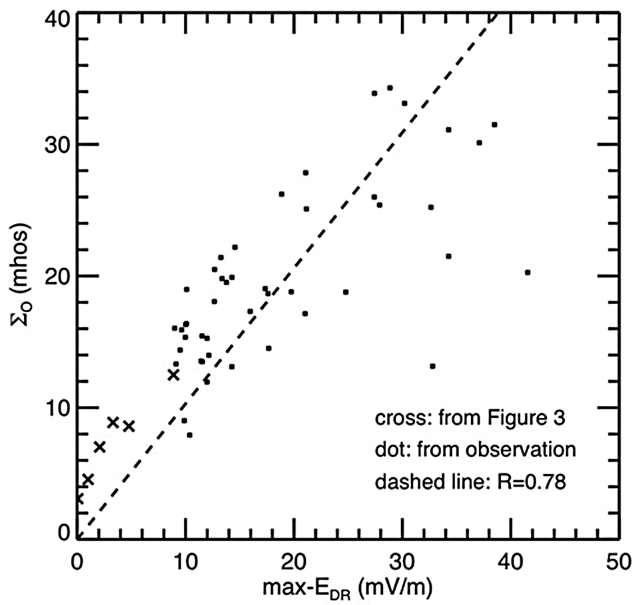

Figure 7. Shows the scatterplot of oval conductance versus E_{DR} obtained by combining (4) with the data for AE in Figure 4 and the data for Φ_{PC} in Figure 5, as described in the text. The scatterplot thus obtained, called the oval conductance, extends the range of E_{DR} from 9 to ~40 mV/m. The dashed line is a linear fit of the scatterplot with correlation coefficient r = 0.78.

[13] Figure 4a shows examples of AE and PCP time series of 10 storm events to illustrate the relationship between max AE and max PCP. Figure 4b shows the distribution of occurrence time difference between max AE and max PCP for 71 storm events. The occurrence time difference between max AE and max PCP for the 71 storm events falls within ~±1 h. The time resolution of polar cap potential is ~1 h.

[14] Figure 5a shows the scatterplot of the observed max AE versus max E_{DR}, where E_{DR} is dayside reconnection E field for the same 71 storm events. Figure 5b shows the distribution of occurrence time difference between max AE and max E_{DR} of the 71 storms is estimated to fall within ~±1 h.

[15] Figure 6a shows the scatterplot of the observed max Φ_{PC} versus max E_{DR} of the same 71 storms. The PCP is based on data from DMSP-F13 spacecraft. The reconnection E field E_{DR} is from the ACE spacecraft. Small to moderate storms with SYMH between −50 and −100 nT are denoted by the "plus" sign; moderate to big storms with SYMH between −100 and −200 nT are denoted by triangles; big to intense storms with SYMH between −200 and −300 nT are denoted by squares; intense to super storms with SYMH between −300 and −500 nT are denoted by crosses. Saturation of PCP is observed to occur statistically in Figure 6a when E_{DR} exceeds ~10 mV/m. Figure 6b shows the distribution of occurrence time difference between max PCP and max E_{DR}. The occurrence time difference falls within ~±1.5 h.

[16] Figure 7 shows the scatterplot of the oval conductance Σ_O versus max E_{DR} obtained by combining (4) with max AE in Figure 5a and max Φ_{PC} in Figure 6a. The dots in Figure 7 are data points for the oval conductance Σ_O for $\alpha \sim 1$ in (4). The crosses in Figure 7 are data points for Σ_O after the LLBL (low-latitude boundary layer) contribution is removed in Figure 3. In other words, the crosses in Figure 7 are obtained by subtracting ~3 mho from Σ_P in Figure 3 so that $\Sigma_P \sim 0$ at $E_{DR} \sim 0$. The scatterplot in Figure 7 can be approximated by a linear fit as shown by the dashed line. The linear correlation coefficient is $R \sim 0.77$. The linear approximation in Figure 7 suggests that the oval conductance increases linearly with increasing E_{DR}. The semiempirical result for the oval conductance shown in Figure 7 can be verified by direct observations in the future.

[17] A nonlinear circuit is characterized by a circuit element, which is a function of the voltage source driving the circuit. The oval conductance Σ_O is a nonlinear circuit element, because it is shown to increases with increasing E_{DR} that drives the SW-M-I coupling circuit. Saturation of polar cap potential in the proposed circuit model depends on the oval conductance being a nonlinear circuit element.

3. Formulation of SW-M-I Coupling Model for Polar Cap Potential Saturation

[18] The proposed quasi-steady SW-M-I coupling circuit model is formulated for the polar cap potential saturation on magnetic storm time scale during southward IMF. Storms and substorms are both driven by enhanced sunward convection in the plasma sheet [*McPherron*, 1970; *Baker et al.*, 1996; *Rostoker*, 2002; *Kan*, 2007]. During the substorm growth phase, sunward convection in the plasma sheet is driven primarily by the enhanced dayside reconnection [*Kan*, 1990], supplemented by reconnection in the mid-to-distant plasma sheet. During substorm expansion phase, sunward convection in the plasma sheet is enhanced primarily by the nightside reconnection driven by the dipolarization-induced NEXL (near-Earth X line) as proposed by *Kan* [2007]. During the storm main phase, sunward convection penetrating deeper into the inner magnetosphere is also driven by dipolarization-induced NEXL as proposed by *Kan et al.* [2007]. Noted that the dipolarization-induced NEXL, formed within a few minutes after dipolarization, is proposed to drive the expanding auroral bulge during substorm expansion phase [*Kan*, 2007]. This is distinctly different from the NEXL proposed to drive BBFs; braking of BBFs is proposed to produce dipolarization in the near-Earth plasma sheet [*Baker et al.*, 1996; *Shiokawa et al.*, 1997; *Angelopoulos et al.*, 2008].

[19] Figure 8 shows the proposed quasi-steady circuit model for the SW-M-I coupling during prolonged southward IMF. The proposed model is intended to describe the polar cap potential saturation during intense magnetic storms. The inductance and capacitance can be omitted in a quasi-steady circuit model. The model consists of the dayside current loop and the nightside current loop coupled by the oval conductance denoted by Σ_O.

[20] The dayside and nightside current loops in Figure 8 are coupled by the oval conductance in that the current in the dayside current loop is driven jointly by both the dayside and nightside reconnection E fields. Likewise, the current in the nightside current loop is also driven jointly by both the dayside and nightside reconnection E fields. Moreover, current in each current loop includes both the region 1 and region 2 field-aligned currents. *Siscoe et al.* [2002]

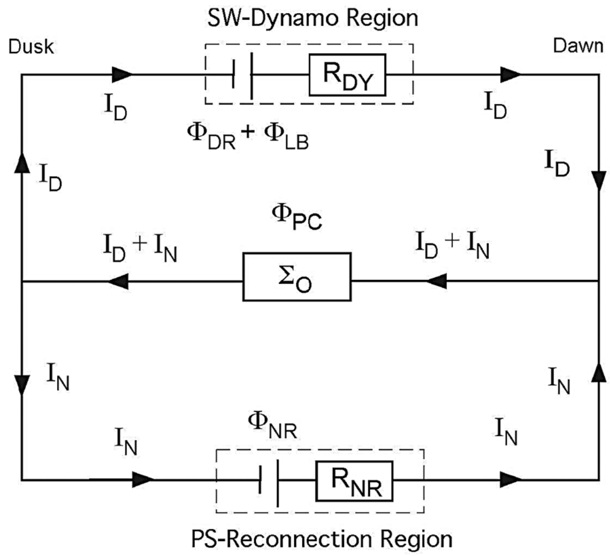

Figure 8. The proposed circuit model of SW-M-I coupling for the polar cap potential saturation. The circuit consists of dayside and nightside current loops. The two current loops are linked by the oval conductance Σ_O in the ionosphere. The solar wind dynamo region in the dayside current loop includes the reconnection potential Φ_{DR}, boundary layer potential Φ_{LB} (negligible compared with Φ_{DR}), and the internal resistance R_{DY} of the dayside reconnection potential representing the collisionless dissipations in the region. The nightside current loop includes the nightside reconnection potential Φ_{NR} and the internal resistance R_{NR} of the reconnection potential, representing collisionless dissipations associated with the reconnection potential driving the sunward convection in the plasma sheet.

choose to consider the region 1 current in their model, while *MacDougall and Jayachandran* [2006] choose to focus on the region 2 current in their model. We choose to consider both the region 1 and region 2 currents in our circuit model.

[21] Release of the magnetic energy stored in the tail lobes is controlled by the reconnection in the plasma sheet. The rate of energy release is determined by the reconnection E field in the plasma sheet, which in turn depends on the location of the reconnection line X line in the plasma sheet. Reconnection rate is greater if the X line is located closer to the Earth [*Kan et al.*, 2007]. Inductance is a passive circuit element, which is replaced by the reconnection E field in the plasma sheet in the proposed quasi-steady nonlinear circuit model in Figure 8.

[22] The SW dynamo consists of BS-MS-MP-BL regions, where BS stands for bow shock, MS for magnetosheath, MP for magnetopause, and BL for low-latitude boundary layer. Global MHD simulations of *Siscoe and Siebert* [2006] and *Guo et al.* [2008] show that bow shock is an integral part of the SW dynamo. Under strongly southward IMF conditions, *Guo et al.* [2008] show that more than 50% of the region 1 field-aligned currents can be traced to the bow shock with the rest traced to the magnetopause.

[23] Solar wind dynamo region consists of the dynamo E field and the dynamo internal resistance. The dynamo E field is the reconnection E field at the dayside magnetopause driven by the solar wind. The internal resistance in the SW dynamo region includes dissipations in the reconnection region, the bow shock, the magnetosheath, and the low-latitude boundary layer, as denoted by R_{DY} in Figure 8.

[24] The nightside reconnection in the plasma sheet converts the magnetic energy in the tail lobes to the electromagnetic energy to enhance the sunward convection. Internal resistance associated with the nightside reconnection potential represents the collisionless dissipation in the plasma sheet, including wave-particle interactions and plasma heating by compression driven by the sunward convection, as denoted by R_{NR} in Figure 8.

[25] During the growth phase, the nightside reconnection X line is located beyond ~$20R_E$ in midtail at MTXL or further down tail, so that the $\Phi_{NR} < \Phi_{DR}$. The solar wind dynamo drives both the dayside and nightside current loops in Figure 8.

[26] During the expansion phase, the nightside reconnection X line is located within ~$20R_E$ in the near-Earth plasma sheet at NEXL. It is possible for $\Phi_{NR} \geq \Phi_{DR}$ so that the oval current is driven jointly by the dayside and nightside reconnection potentials. In this case, the dayside and nightside current loops in Figure 8 are driven jointly by the dayside and nightside reconnection potentials.

[27] The governing equations for the proposed quasi-steady SW-M-I coupling circuit in Figure 8 can be written as

$$\Phi_{DR} + \Phi_{LB} = \Phi_{PC} + I_D R_{DY}, \tag{5}$$

$$\Phi_{PC} = (I_D + I_N)/\Sigma_O, \tag{6}$$

$$\Phi_{NR} = \Phi_{PC} + I_N R_{NR}. \tag{7}$$

Substituting (5) and (7) into (6), yields

$$\begin{aligned}(\Sigma_O + 1/R_{DY} + 1/R_{NR})\Phi_{PC} = (\Phi_{DR} + \Phi_{LB})/R_{DY} \\ + \Phi_{NR}/R_{NR}.\end{aligned} \tag{8}$$

Equation (8) can be written as

$$\begin{aligned}&[1 + (\Sigma_O R_{DY}) + (R_{DY}/R_{NR})]\Phi_{PC} \\ &\quad = (\Phi_{DR} + \Phi_{LB}) + (R_{DY}/R_{NR})\Phi_{NR}.\end{aligned} \tag{9}$$

Here we introduce simplifying assumptions that $\Phi_{DR} \gg \Phi_{LB} \sim 20$ kV during prolonged southward IMF. Neglecting Φ_{LB} in (9), the polar cap potential can be written as

$$\Phi_{PC} = [\Phi_{DR} + (R_{DY}/R_{NR})\Phi_{NR}]/[1 + (\Sigma_O R_{DY}) + (R_{DY}/R_{NR})]. \tag{10}$$

Let Φ_R be the combined dayside/nightside reconnection potential, as defined by the numerator of (10), i.e.,

$$\begin{aligned}\Phi_R &\equiv [\Phi_{DR} + (R_{DY}/R_{NR})\Phi_{NR}] \\ &= \Phi_{DR}(1 + \beta\gamma).\end{aligned} \tag{11}$$

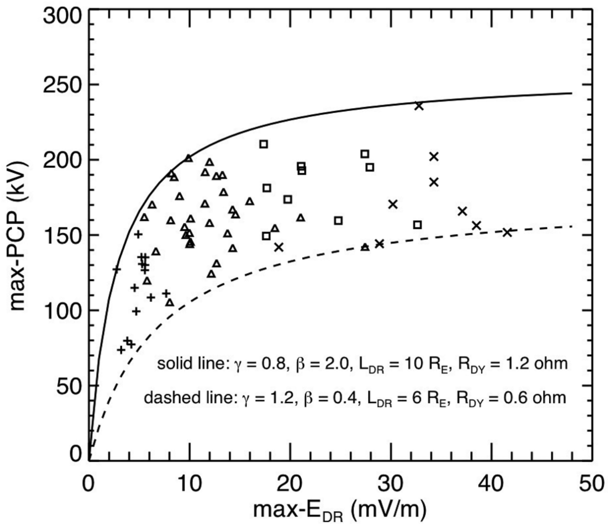

Figure 9. Comparing model predictions with data of polar cap potential saturation of 71 storms. The scatterplot of observed data is identical to that shown in Figure 5. The model predictions are shown by the curves. The solid curve is for $\beta(=\Phi_{NR}/\Phi_{DR}) = 2.0$, $\gamma\ (=R_{DY}/R_{NR}) = 0.8$, $L_{DR} = 10R_E$, and $R_{DY} = 1.2$ ohm. The dashed curve is for $\beta = 0.4$, $\gamma = 1.2$, $L_{DR} = 6R_E$, and $R_{DY} = 0.6$ ohm. These parameter values are chosen so that the data in Figure 8 are bounded by the curves of the model prediction.

The polar cap potential in (10) can be reduced to

$$\Phi_{PC} = \Phi_R/[1 + (\Sigma_O R_{DY}) + (R_{DY}/R_{NR})], \qquad (12)$$

where $\beta \equiv \Phi_{NR}/\Phi_{DR}$ and $\gamma \equiv R_{DY}/R_{NR}$ are dimensionless parameters of the proposed SW-M-I coupling model for the polar cap potential.

[28] The reconnection potential in (11) can be rewritten in terms of E_{DR} as

$$\Phi_R = (1 + \beta\gamma)L_{DR}E_{DR}, \qquad (13)$$

where L_{DR} in (13) is the length of dayside reconnection line and E_{DR} is the dayside reconnection E field given by (1).

[29] Sunward convection in the plasma sheet is significantly enhanced during substorm expansion phase [*Kan*, 2007] and during the storm main phase [*Kan et al.*, 2007] driven by the dipolarization-induced NEXL (near-Earth X line) in the plasma sheet to enhance the nightside reconnection potential. Enhancing the nightside reconnection is a response to reducing the imbalance between the open flux and closed flux in the magnetosphere. Open field lines are accumulated in the tail lobes by the dayside reconnection during southward IMF, at the same time, depleting closed field lines in the magnetosphere. Enhanced nightside reconnection at NEXL is no doubt related to the enhanced dayside reconnection. Two schools of thoughts on the cause of reconnection in the plasma sheet have been proposed. One school suggests that reconnection in the plasma sheet is determined exclusively by the condition in the plasma sheet [e.g., *Baker et al.*, 1996; *Shiokawa et al.*, 1997; *Angelopoulos et al.*, 2008]; the other school believes that reconnection in the near-Earth plasma sheet is caused by the closure of Cowling electrojet current to produce dipolarization around ~10 R_E leading to the dipolarization-induced NEXL to drive the expanding auroral bulge during the substorm expansion phase [*Kan*, 2007]. This issue is still a topic of ongoing debate in substorm and storm research.

[30] The oval conductance, approximated by the dashed line in Figure 7, can be written as

$$\Sigma_O = \kappa\ E_{DR}, \qquad (14)$$

where $\kappa \sim 0.56$ mho/(mV/m) according to Figure 7. Substituting (12) for Φ_R and (14) for Σ_O into (11), the polar cap potential can be rewritten as

$$\Phi_{PC} = (1 + \beta\gamma)L_{DR}E_{DR}/(1 + \gamma + \kappa\ E_{DR}R_{DY}). \qquad (15)$$

As $(\kappa E_{DR}R_{DY}) \gg (1 + \gamma)$, the polar cap potential in (15) approaches the asymptotic saturation potential Φ_{AS} obtained from (15) as

$$\Phi_{AS} = (1 + \beta\ \gamma)L_{DR}/(\kappa R_{DY}). \qquad (16)$$

[31] Figure 9 shows comparison of the prediction of proposed SW-M-I circuit model with observed polar cap potential of 71 storms. The scatterplot are identical to that shown in Figure 6a. The model predictions are shown by curves. The solid curve is for $\beta(=\Phi_{NR}/\Phi_{DR}) = 2.0$, $\gamma\ (=R_{DY}/R_{NR}) = 0.8$, $L_{DR} = 10R_E$, and $R_{DY} = 1.2$ ohm. The dashed curve is for $\beta = 0.4$, $\gamma = 1.2$, $L_{DR} = 6R_E$, and $R_{DY} = 0.6$ ohm. These two sets of parameter values are chosen so that the data in Figure 9 are bounded by the model prediction curves.

[32] Figure 10 explores the effect of changing each of the four parameters while keeping other parameters fixed in the proposed SW-M-I coupling model. Figure 10a shows the saturation potential increases with decreasing internal dynamo resistance R_{DY} while keeping the other parameters fixed. Figure 10b shows the saturation potential increases with increasing length of dayside reconnection line L_{DR} while keeping the other parameters fixed. Figure 10c shows the saturation potential increases with increasing $\beta(=\Phi_{NR}/\Phi_{DR})$ while keeping other parameters fixed. Figure 10d shows the saturation potential increases with increasing $\gamma\ (=R_{DY}/R_{NR})$ while keeping the other parameters fixed.

4. Discussion and Conclusion

[33] We strive to keep the proposed SW-M-I quasi-steady circuit model as simple as possible, retaining only the essential circuit elements of fundamental importance to the observed saturation of polar cap potential. The model is developed for the storm time scale of several tens of hours to a few days. The storm time scale is much longer than the substorm time scale of less than a few hours. Transient phenomena on the substorm time scale are thus excluded. The essential elements in the proposed circuit model are the dynamo potential and its internal resistance; the NEXL reconnection potential in the near-Earth plasma sheet and its internal resistance; the oval conductance produced by precipitating electrons and ions energized by enhanced convection driven by the dayside reconnection at the magnetopause and the NEXL reconnection in the plasma sheet, all driven by the solar wind.

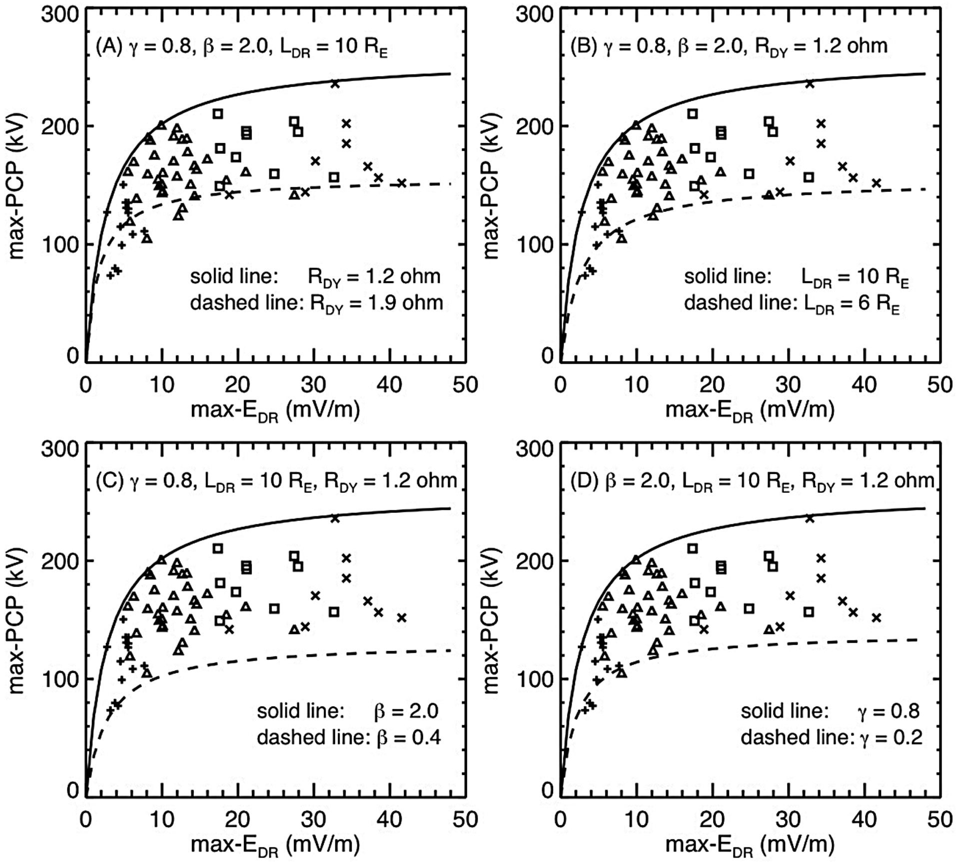

Figure 10. Effect of each of the four parameters on the polar cap potential. (a) The saturation potential increases with decreasing internal resistance R_{DY} in the dynamo region while keeping the other parameters fixed. (b) The saturation potential increases with increasing length of dayside reconnection line L_{DR} while keeping the other parameters fixed. (c) The saturation potential increases with increasing $\beta(=\Phi_{NR}/\Phi_{DR})$ while keeping other parameters fixed. (d) The saturation potential increases with increasing $\gamma(=R_{DY}/R_{NR})$ while keeping the other parameters fixed.

[34] The internal resistance associated with the reconnection process can be attributed to the collisionless dissipation driven by the reconnection potential. The internal resistance regulates the net potential output by the SW dynamo and the net potential output by the nightside reconnection in the plasma sheet. The collisionless dissipation in the SW dynamo region includes wave-particle interactions and compressional plasma heating in the bow shock and in the magnetosheath. Likewise, the collisionless dissipation in the plasma sheet is associated with wave-particle interactions and compressional plasma heating driven by the sunward convection driven by reconnection in the plasma sheet. Quantitative estimate of the collisionless dissipation is beyond the scope of the present paper. By comparing model predictions with observations of polar cap potential saturation, we will present an order of magnitude estimate of the internal resistance. A quantitative determination of the internal resistance is beyond the scope of the present paper.

[35] In conclusion, we show that the observed polar cap potential saturation can be understood as caused by nonlinearity in the SW-M-I coupling driven by the solar wind. Nonlinearity in the proposed SW-M-I circuit model originates from the dependence of oval conductance on the dayside reconnection E field. Saturation of the polar cap potential depends on the three essential circuit elements:

[36] 1. The oval conductance Σ_O increases linearly with increasing E_{DR} as shown in Figure 7. Nonlinearity of the SW-M-I coupling for the polar cap potential saturation is shown to originates from the oval conductance Σ_O increases linearly with increasing E_{DR}.

[37] 2. The combined dayside/nightside reconnection potential Φ_R in (12) is driven by the solar wind, which in turn drives the storms and substorms.

[38] 3. The asymptotic saturation potential is predicted to increase with (1) decreasing internal resistance in the dynamo region; (2) increasing length of dayside reconnection line; (3) increasing ratio of nightside to dayside reconnection potential; and (4) increasing ratio of nightside to dayside internal resistance in the reconnection region.

[39] The linear Σ_O-E_{DR} relationship shown in Figure 7 is a semiempirical result deduced from observations to be verified by direct observations in the future.

[40] **Acknowledgments.** This research is supported in part by the National Natural Science Foundation of China (40831060) and the Specialized Research Fund for State Key Laboratories in China. One of us (J. R. Kan) is

also supported in part by the HAARP project under ONR award N00014-08-1-0439 to the Geophysical Institute, University of Alaska Fairbanks. An email exchange with Professor George Siscoe is greatly appreciated.

[41] Zuyin Pu thanks the reviewers for their assistance in evaluating this paper.

References

Angelopoulos, V., et al. (2008), Tail reconnection triggering substorm onset, *Science*, *321*, 931–935, doi:10.1126/science.1160495.

Baker, D. N., T. I. Pulkkinen, V. Angelopoulos, W. Baumjohann, and R. I. McPherron (1996), Neutral line model of substorms: Past results and present view, *J. Geophys. Res.*, *101*(A6), 12,975–13,010.

Block, L. P., C.-G. Falthammar, P. Rothwell, and M. B. Silevitch (1998), Advantages of electric circuit models for treating the substorm breakup problem, *J. Geophys. Res.*, *103*(A4), 6913–6916, doi:10.1029/97JA03684.

Boyle, C. B., P. H. Reiff, and M. R. Hairston (1997), Empirical polar cap potentials, *J. Geophys. Res.*, *102*(A1), 111–125.

Doyle, M. A., and W. J. Burke (1983), S3-2 measurements of the polar cap potential, *J. Geophys Res.*, *88*(A11), 9125–9133.

Fedder, J. A., and J. G. Lyon (1987), The solar wind-magnetosphere-ionosphere current-voltage relationship, *Geophys. Res. Lett.*, *14*(8), 880–883, doi:10.1029/GL014i008p00880.

Guo, X. C., C. Wang, Y. Q. Hu, and J. R. Kan (2008), Bow shock contributions to region 1 field-aligned current: A new result from global MHD simulations, *Geophys. Res. Lett.*, *35*, L03108, doi:10.1029/2007GL032713.

Hairston, M. R., T. W. Hill, and R. A. Heelis (2003), Observed saturation of the ionospheric polar cap potential during the 31 March 2001 storm, *Geophys. Res. Lett.*, *30*(6), 1325, doi:10.1029/2002GL015894.

Hairston, M. R., K. A. Drake, and R. Skoug (2005), Saturation of the ionospheric polar cap potential during the October–November 2003 superstorms, *J. Geophys. Res.*, *110*, A09S26, doi:10.1029/2004JA010864.

Hardy, D. A., M. S. Gussenhoven, R. Raistrick, and W. J. McNeil (1987), Statistical and functional representations of the pattern of auroral energy flux, number flux, and conductivity, *J. Geophys. Res.*, *92*(A11), 12275–12294.

Hill, T. W. (1984), Magnetic coupling between solar wind and magnetosphere: Regulated by ionospheric conductance?, *Eos Trans. AGU*, *65*, 1047–1048.

Kan, J. R. (1990), Tail-like reconfiguration of the plasma sheet during the substorm growth phase, *Geophys. Res. Lett.*, *17*(13), 2309–2312, doi:10.1029/GL017i013p02309.

Kan, J. R. (2007), On the formation of near-Earth X line at substorm expansion onset, *J. Geophys. Res.*, *112*, A01207, doi:10.1029/2006JA012011.

Kan, J. R., and L. C. Lee (1979), Energy coupling function and solar wind-magnetosphere dynamo, *Geophys. Res. Lett.*, *6*(7), 577–580, doi:10.1029/GL006i007p00577.

Kan, J. R., X. Xing, and R. A. Wolf (2007), Intensity of geomagnetic storms depends on the X line location in the plasma sheet, *J. Geophys. Res.*, *112*, A04216, doi:10.1029/2006JA011945.

Kivelson, M. G., and A. J. Ridley (2008), Saturations of the polar cap potential: Inference from Alfvén wing, *J. Geophys. Res.*, *113*, A05214, doi:10.1029/2007JA012302.

Liu, Z. X., L. C. Lee, C. Q. Wei, and S. I. Akasofu (1988), Magnetospheric substorms: An equivalent circuit approach, *J. Goephys. Res.*, *93*(A7), 7366–7375.

Lockwood, M., M. Hairston, I. Finch, and A. Rouillard (2009), Transpolar voltage and polar cap flux during the substorm cycle and steady convection events, *J. Geophys. Res.*, *114*, A01210, doi:10.1029/2008JA013697.

MacDougall, J. W., and P. T. Jayachandran (2006), Polar cap voltage saturation, *J. Geophys. Res.*, *111*, A12306, doi:10.1029/2006JA011741.

McPherron, R. L. (1970), Growth phase of magnetospheric substorms, *J. Geophys. Res.*, *75*(28), 5592–5599, doi:10.1029/JA075i028p05592.

Merkin, V. G., A. S. Sharma, K. Papadopoulos, G. Milikh, J. Lyon, and C. Goodrich (2005), Global MHD simulations of the strongly driven magnetosphere: Modeling of the transpolar potential saturation, *J. Geophys. Res.*, *110*, A09203, doi:10.1029/2004JA010993.

Reiff, P. H., and J. G. Luhmann (1986), Solar wind control of the polar-cap potential, in *Solar Wind-Magnetosphere Coupling*, edited by Y. Kamide and J. A. Slavin, p. 453, Terra Sci., Tokyo.

Reiff, P. H., R. W. Spiro, and T. W. Hill (1981), Dependence of polar cap potential drop on interplanetary parameters, *J. Geophys. Res.*, *86*(A9), 7639–7648.

Ridley, A. J. (2005), A new formulation for the ionospheric cross polar cap potential including saturation effects, *Ann. Geophys.*, *23*, 3533–3547.

Rostoker, G. (2002), Identification of substorm expansion phase onsets, *J. Geophys. Res.*, *107*(A7), 1137, doi:10.1029/2001JA003504.

Russell, C., J. Luhmann, and G. Lu (2001), The non-linear response of the polar ionosphere to large values of the interplanetary electric field, *J. Geophys. Res.*, *106*(A7), 18,495–18,504.

Sato, T., and T. E. Holzer (1973), Quiet auroral arcs and electrodynamics coupling between the ionosphere and the magnetosphere, I, *J. Geophys. Res.*, *78*(31), 7314–7329.

Shepherd, S. G. (2007), Polar cap potential saturation: Observations, theory, and modeling, *J. Atmos. Sol.-Terr. Phys.*, *69*, 234–248.

Shepherd, S. G., J. M. Ruohoniemi, and R. A. Greenwald (2003), Testing the Hill model of transpolar potential using Super Dual Auroral Radar Network observations, *Geophys. Res. Lett.*, *30*(1), 1002, doi:10.1029/2002GL015426.

Shiokawa, K., W. Baumjohann, and G. Haerendel (1997), Braking of high-speed flows in the near-Earth tail, *Geophys. Res. Lett.*, *24*(10), 1179–1182, doi:10.1029/97GL01062.

Siscoe, G. L. (1982), Energy coupling between regions 1 and 2 Birkeland currents, *J. Geophys. Res.*, *87*(A7), 5124–5130.

Siscoe, G. L., and K. D. Siebert (2006), Bimodal nature of solar wind-magnetosphere-ionosphere-thermosphere coupling, *J. Atmos. Sol.-Terr. Phys.*, *68*, 911–920.

Siscoe, G. L., G. M. Erickson, B. U. O. Sonnerrup, N. C. Maynard, J. A. Schoendorf, K. D. Siebert, D. R. Weimer, W. W. White, and G. R. Wilson (2002), Hill model of transpolar potential saturation: Comparisons with MHD simulations, *J. Geophys. Res.*, *107*(A6), 1075, doi:10.1029/2001JA000109.

Siscoe, G. L., et al. (2004), Transpolar potential saturation models compared, *J. Geophys. Res.*, *109*, A09203, doi:10.1029/2003JA010318.

Y. Q. Hu, CAS Key Laboratory of Basic Plasma Physics, School of Earth and Space Sciences, University of Science and Technology of China, Hefei, Anhui 230026, China.

J. R. Kan, H. Li, B. B. Tang, and C. Wang, State Key Laboratory of Space Weather, Center for Space Science and Applied Research, Chinese Academy of Sciences, 1 NanErTiao, ZhongGuanCun, PO Box 8701, Beijing 100190, China. (joe.kan@gi.alaska.edu)